geoconvention
Calgary • Canada • May 13-17 2019

Attenuation tomography using recorded microseismicity in a mine

Himanshu Barthwal[1], Frank J. Calixto[2], and Mirko van der Baan[1]
[1]University of Alberta, Canada, [2]Institute of Mine Seismology, Australia

Summary

We perform three-dimensional attenuation tomography using microseismic data recorded during an underground mine development. The whole path attenuation parameter t^* is obtained by least-squares inversion of P-wave amplitude spectra of the events recorded by 7 monitoring wells each containing 4 3C geophones. For tomographic inversion, we use 292 events out of the total 488 identified events for which the corner frequencies ranged between 120 to 210 Hz. The inverted quality factor Q varies between 9 to 100 with the event cluster location characterized by low Q value of 10. Two high Q regions of 45-55 are located, one between 0 to 0.2 km East and 0.3 to 0.5 km North, and another centered around 0.5 km East and 0.25 km North. The high (-low) Q values show a good correlation with the high (-low) velocities present in the velocity tomography model. Thus, the attenuation model can reveal heterogeneity present within the mine thereby providing valuable geological insights in regions not accessible for direct sampling.

Introduction

Microseismic monitoring is often employed in underground mines to detect anomalous seismicity to ensure safe mining operations. Recent studies (Westman et al., 2012; Barthwal and Van der Baan, 2019) have performed velocity tomography using the recorded microseismicity to obtain 3D velocity models of the mines. Similarly, the microseismic recordings can be used to obtain 3D seismic attenuation models that can provide additional insights about rock properties like lithology, fracture density, and fluid contents.

In this study, we use the microseismic data acquired during an underground mining development for a period of one month during January 2011. The mine is located in Saskatchewan, Canada. The data were recorded by a network of 7 boreholes each having 4 3C geophones at a sampling rate of 500 samples per second. These data have been studied previously by Castellanos and Van der Baan (2013, 2015) and Barthwal and Van der Baan (2019) who give details of the microseismic data processing and mine geology.

Figure 1a shows a schematic North-South cross-section through the mine. The ore deposition is along an unconformity contact between sandstone and the underlying basement rock gneiss at a depth of nearly 450 m. Figure 1a shows many faults in the basement rock and the overlying sandstones which may have lead to ore deposition due to fluids flowing through them (Fayek, 2013). There are two vertical shafts to access the horizontal tunnel networks at depths of 420 m, 465 m, 480 m, and 500 m. Figure 1b displays the 488 microseismic events located by Barthwal and Van der Baan (2019), the receiver locations used for data recording, and the 3D distribution of mapped faults. The two largest multiplet groups namely group 1 and group 3 containing 179 and 38 events are shown by red filled spheres and the green filled cubes respectively. The multiplet groups are tightly clustered near the 480 m level and shaft 1. The remaining 271 events are shown by gray filled spheres. The dominant faults are striking in the East-West direction. Fault orientations along NW-SE, NNW-SSE, N-S, and NE-SW directions are also present in the region.

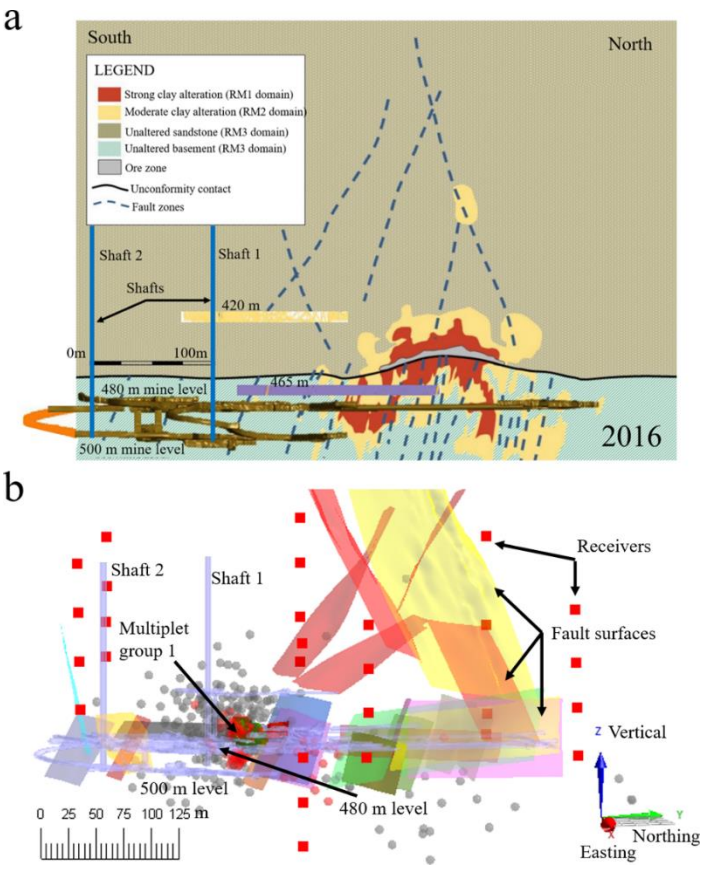

Figure 1: (a) Schematic North-South cross-section through the mine showing the shafts and tunnel layout, inferred faults, and the geotechnical zones (Courtesy: anonymous company). (b) 3D view of the shafts and tunnel layout, mapped faults (shown as colored surfaces), receiver locations (red filled squares). Red filled spheres show the event locations of multiplet group 1, green filled cubes correspond to the event locations of multiplet group 3, gray filled spheres show remaining event locations. Event locations are taken from Barthwal and Van der Baan (2019).

Method

Spectral fitting for t^* estimation

We fit the amplitude spectra of the recorded waveforms assuming a Brune's source model (Brune, 1970) for the microseismic events. Taking into account the attenuation during wave propagation, the velocity spectral amplitude A_{ij} of an event i at a receiver j for a frequency f is given as

$$A_{ij}(f) = 2\pi f \Omega_{0i} I_j G_{ij} R_j \frac{f_{ci}^2}{f_{ci}^2+f^2} \exp[-\pi f t_{ij}^*], \quad (1)$$

where Ω_{0i} and f_{ci} are the low-frequency spectral amplitude and corner frequency of event i. I_j, R_j, and G_{ij} are the instrument response, receiver site effect and the geometrical spreading respectively. t_{ij}^* is the whole path attenuation for the ray propagating from event i to receiver j. t_{ij}^* represents the cumulative spatial effect of attenuation along the ray path from event i to receiver j and is given as (Scherbaum, 1990; Scherbaum and Wyss, 1990; Lees and Lindley, 1994)

$$t_{ij}^* = \int_i^j \frac{dr(x,y,z)}{Q(x,y,z)v(x,y,z)}, \quad (2)$$

where $dr(x,y,z)$ is a small ray path element, $Q(x,y,z)$ and $v(x,y,z)$ are the Quality factor and velocity at any spatial point (x,y,z) along the ray path. The integration is carried out along the ray path from source to receiver locations.

Taking the natural logarithm of equation 1 after substituting $\Omega_{0i} I_j G_{ij} R_j$ by Ω'_{0ij}, and rearranging, we get

$$\ln A_{ij}(f) - \ln 2\pi f - \ln \frac{f_{ci}^2}{f_{ci}^2+f^2} = \ln \Omega'_{0ij} - \pi f t_{ij}^*, \quad (3)$$

where the left-hand side is known for a given frequency f and a test corner frequency f_{ci}. Ω'_{0ij} on the right-hand side is the signal moment including all frequency independent amplification factors (spectral moment, geometrical spreading, instrument gain, and frequency independent site response) (Haberland and

Rietbrock, 2001). Equation 3 can be solved for $\ln \Omega'_{0ij}$ and t^*_{ij} for an event i recorded at receivers $j = 1, 2, 3, \ldots\ldots, nr$.

We constrain the corner frequency by taking a single value for all observations of an event i.e. a constant f_{ci} for an event i recorded at receivers $j = 1, 2, 3, \ldots\ldots, nr$. The test frequency f_{ci} used in equation 3 is selected from an expected range of corner frequencies. The best estimate of the corner frequency is then obtained by a grid search for the test corner frequency which minimizes a misfit function between modeled and observed spectra.

3D Q tomography

The whole path attenuation t^*_{ij} in equation 2 can be discretized to create a tomography approach. Assuming that the event locations and 3D velocity model are known, equation 2 can be set up as a linear inverse problem for Q^{-1} by discretizing the model domain as

$$t^*_{ij} = \sum_{n=1}^{K} \left(\frac{r_n}{v_n}\right) Q_n^{-1}\,, \qquad (4)$$

where the ray path is divided into K segments, r_n, v_n, and Q_n are the path length, velocity, and the Quality factor of the nth segment. Equation 4 can be solved for the model parameters Q_n^{-1} using a damped least-squares method. The data vector contains t^*_{ij} measurements obtained from spectral fitting described in the previous subsection.

Results

Figure 2 shows the velocity spectral fitting for the t^*_{ij} estimation. The vertical red lines mark the 28 ms window used to compute the P-wave amplitude spectrum shown by the red curve on the right panel. The 7 frequency samples corresponding to the 14 sample length input time series are displayed on top of the red curve and marked by 'star' symbol. The green curves on the right panel show the pre-arrival noise spectrum. The thick blue lines show the best-fitting theoretical spectra obtained using equation 1 from the computed t^*_{ij}, and f_c. The blue curve gives a reasonable fit to the observed signal spectrum for all 3 events shown in Figure 2. For the 488 events, the dominant corner frequency is 170 Hz; however, there is considerable scatter with some frequencies as low as 40 Hz. The maximum amplitudes of all recorded microseismic events are at least three orders of magnitude less than those of the mine blasts. So, their moment magnitudes are most likely to be negative (Barthwal and Van der Baan, 2019). The Nyquist frequency for the recorded data is 250 Hz; however, microseismic events with negative magnitudes are known to have corner frequencies greater 250 Hz possibly up to few kHz (Kwiatek et al., 2011; Eisner et al., 2013). In order to avoid errors in attenuation tomography due to low sampling rate, we use 292 events out of the total 488 identified events with corner frequencies between 120 and 210 Hz.

Next, we perform 3D Q tomography by damped least-squares inversion of equation 4 set up for all 292 events using the t^* measurements obtained from spectral fitting. We assume an initial homogeneous attenuation model with Q=30. A damping parameter of 0.02 is selected from the tradeoff curve between data and model variance. Figure 3 shows the various horizontal and vertical cross-sections through the inverted 3D Q model obtained from attenuation tomography. The Q values range from 9 to 100. At Z=0.4 and 0.45 km, there is a low Q value of 10 centered at 0.2 km North and between 0.2 to 0.25 km East. This low Q correlates well with low velocity in this region obtained by Barthwal and Van der Baan, 2019. There are two high Q regions at Z=0.5 km, one between X=0 to 0.2 km and Y=0.3 to 0.6 km. The other high Q region around X=0.5 km and Y=0.25 km is also present in the depth sections at Z=0.4 and 0.45 km. The different North-South cross sections at X=0.2, 0.25 and 0.3 km are displayed in the middle panel. A low Q region between depths of 0.35 to 0.55 km is centered around Y=0.2 km. There is a lateral Q variation with a high Q region towards North between depths of 0.4 to 0.55 km and Y=0.25 to 0.4 km for all the North-South cross-sections. Similar Q contrasts can be seen in the East-West cross sections shown in the lower panel with the low Q region spanning depths of 0.35 to 0.55 km and between X=0.2 to 0.3 km. The low (-high) Q values show a good correlation with the low (-high) velocity regions present in the velocity model of Barthwal and Van der Baan, 2019.

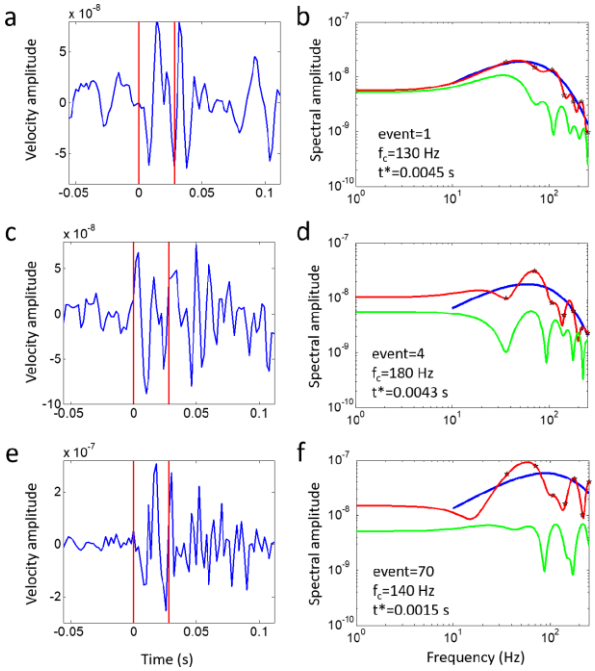

Figure 2: Spectral fitting of recorded waveforms of the microseismic events at different receivers. The left panel shows the microseismic waveforms rotated along the ray propagation direction (a, c, e). The vertical lines show the signal window of 28 ms containing the P-wave arrival. The right panel shows the signal spectra (red curve), noise spectra (green curve) and the best fitting theoretical spectra (thick blue curve). The 'star' symbol represents the 7 frequency samples corresponding to the 14 sample length input time series. The event number, estimated corner frequency f_c, and t^* are displayed in the lower left corner (b, d, f).

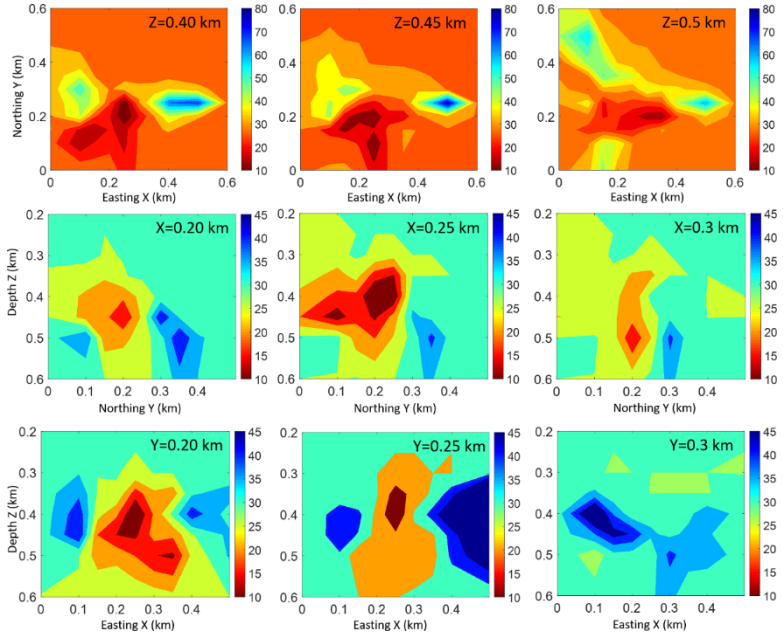

Figure 3: 3D Q model obtained from tomographic inversion of field data. Top panel: Map view at depths of 0.4, 0.45, and 0.5 km displayed on top right corner. Middle panel: North-South cross-sections at Easting X=0.2, 0.25, and 0.3 km displayed on top right corner. Lower panel: East-West cross-sections at Northing Y=0.2, 0.25, and 0.3 km displayed on top right corner.

Conclusions

Three-dimensional Q model is obtained for an underground mine using the t^* measurements from amplitude spectra of microseismic events. The Q model shows lateral heterogeneity with low Q values near the microseismic event clusters around X=0.2 km, Y=0.2 km and between depths of 0.4 to 0.5 km. The low and high Q values correlate well with the low and high seismic velocities. Thus, attenuation tomography using recorded microseismicity can yield information beyond the event locations and can be a great aid in geological interpretation.

Acknowledgments

We thank Fernando Castellanos for preprocessing of the microseismic dataset. We would also like to thank an anonymous company for permission to use and show the dataset, and the sponsors of the Microseismic Industry Consortium for project funding.

References

Brune, J. N., 1970, Tectonic stress and the seismic shear waves from earthquakes: J. Geophys. Res., 75, 4997-5009.

Barthwal, H., and M. Van der Baan, 2019, Passive seismic tomography using recorded microseismicity: Application to mining-induced seismicity: Geophysics, 84, in press.

Castellanos, F., and M. Van der Baan, 2013, Microseismic event locations using the double-difference algorithm: CSEG Recorder, 38(3), 26-37.

Castellanos, F., and M. Van der Baan, 2015, Dynamic Triggering of Microseismicity in a mine setting: Geophysical Journal International, 202(2), 728-737.

Eisner L., D. Gei, M. Hallo, I. Opršal, M. Y. Ali, 2013, The peak frequency of direct waves for microseismic events: Geophysics, 78(6), A45-A49.

Fayek, M., 2013, Uranium Ore Deposits: A review. In Uranium: Cradle to Grave, (eds. P.C. Burns and G. Sigmon), Mineralogical Association of Canada, 43, 121-147.

Haberland, C., and A. Rietbrock, 2001, Attenuation tomography in the western central Andes: a detailed insight into the structure of a magmatic arc: J. Geophys. Res., 106, 11,151-11,167.

Kwiatek, G., K. Plenkers, and G. Dresen, 2011, Source parameters of picoseismicity recorded at Mponeng Deep Gold Mine, South Africa: Implications for Scaling Relations: Bulletin of the Seismological Society of America, 101(6), 2592--2608.

Lees, J. M., and G. T. Lindley, 1994, Three-dimensional attenuation tomography at Loma Prieta: Inversion of t* and Q: J. Geophys. Res., 99, 6843--6863.

Scherbaum, F., 1990, Combined inversion for the three-dimensional Q structure and source parameters using microearthquake spectra: J. Geophys. Res., 95, 12,423--12,438.

Scherbaum, F., and M. Wyss, 1990, Distribution of Attenuation in the Kaoiki, Hawaii, Source Volume Estimated by Inversion of P Wave Spectra: J. Geophys. Res., 95, 12,439--12,448.

Westman, E., K. Luxbacher, and S. Schafrik, 2012, Passive seismic tomography for three-dimensional time-lapse imaging of mining-induced rock mass changes: The Leading Edge, 31(3), 338--345.